Mechanics of Strain-limiting wrinkled kirigami for flexible devices: High flexibility, stretchability and compressibility

Yafei Wang [a,1], Changguo Wang [a,b,*,1]

[a] National Key Laboratory of Science and Technology for National Defence on Advanced Composites in Special Environments, Harbin Institute of Technology, Harbin 150001, PR China
[b] Center for Composite Materials, Harbin Institute of Technology, Harbin 150001, PR China

ABSTRACT

Flexible devices that provide elastic responses to ultrahigh deformations are of growing interest due to the ability to enable new applications whose feasibility is impossible to be attained by using the traditional wafer-based technologies. This paper focuses on strain-limiting wrinkled kirigami materials that offer coexistent high flexibility, stretchability and compressibility, as well as its mechanics design strategies that can be suitable for both discrete and distributed flexible systems, enabling them to accommodate extreme mechanical deformations without damage, such as stretching, compressing and twisting like a rubber ribbon. Comprehensive and systematic theoretical studies of the mechanics reveal how to leverage the different dimensionless geometric parameters to regulate buckling responses of the system, such as global buckling and local wrinkling, and the way in which the parameterized designs enable highly parallel extreme mechanical properties. To some extent, flexibility, stretchability and compressibility can be enhanced by several orders of magnitude, except for some counterintuitive expectations. The predicted results, as validated and demonstrated through in-situ tensile experiments and numerical calculations, provide an underpinning to unveil the concealed relationships between nonlinear mechanics responses and microstructural geometries as well as material properties of strain-limiting wrinkled kirigami. This paper suggests a promising route to high-performance flexible devices regarding the stretchable conductors and piezoelectric harvesters.

1. Introduction

Recent developments in materials and mechanics for flexible devices (Jiang et al., 2007; Khang et al., 2006; Kim et al., 2008b; Rogers et al., 2010; Wang et al., 2012; Yang and Suo, 2018) enable electronic systems with high-performance circuit operating and integration densities can be achieved in mechanics that showcases dramatic deformation without affecting electronical functionaries, e.g., stretching, compressing and twisting like a rubber ribbon. The derived technology lines shed light on a wide range of application opportunities that cannot be addressed with conventional rigid electronics, from epidermal wellness monitors (Chung et al., 2020; Jeong et al., 2013; Kim et al., 2011; Yeo et al., 2013), to sensitive artificial skins (Mannsfeld et al., 2010; Someya et al., 2004; Wagner et al., 2004), and to soft thermal/electric conductors (Guan et al., 2018; Jang et al., 2017; Ma et al., 2018; Shyu et al., 2015). Meanwhile, two particularly successful design forms, including

discrete and distributed design paradigms (Rogers et al., 2010), have been refined to achieve the integrated flexible systems and engineered elasticity (Callens and Zadpoor, 2018). For the first form, stretchable systems exploit island-bridge architectures (Ko et al., 2008; Lu and Yang, 2015; Song et al., 2016; Zhang et al., 2015a), in which active components are distributed in the localized, rigid and functional platform as islands, and are joined by deformable electrical/mechanical interconnects as bridges. During the stretching process, relatively stiff islands can effectively provide mechanics shielding for brittle active components, to prevent strains that could cause rupture (Zhang et al., 2013). Moreover, the bridges are strongly responsible for high flexibility and stretchability that can be realized through typically strategic designs of interconnects, such as serpentine design, fractal/self-similar inspired design, helical structural design and origami/kirigami inspired design (Liu et al., 2016; Ma et al., 2017; Song, 2015; Song et al., 2016; Xu et al., 2015b; Zhang et al., 2015a). For the second form, that is, the distributed

---

* Corresponding author.
  E-mail address: wangcg@hit.edu.cn (C. Wang).
[1] These authors contributed equally to this work.

design paradigm, high flexibility, stretchability and compressibility are achieved directly in thin films of high-quality, single-crystal inorganic semiconductors (such as silicon) that have periodic, wave-like geometries (Jiang et al., 2007; Khang et al., 2006; Kim et al., 2008a; Rogers et al., 2010; Sun et al., 2006; Wang et al., 2008). Such prestrain (or compressive strain) controlled flexible systems with fully distributed wrinkled film on compliant substrates overcome the functional mismatch of biology and silicon wafers in mechanics. As under stretching conditions, the surface wrinkles of bilayer systems will unfold to accommodate the system-level deformation, the designs represent, then, a form of silicon with a strain range of 10 to 20%, that is, 10 to 20 times as large as the intrinsic fracture limits of the silicon (Rogers et al., 2010). Actually, buckling of thin, stiff films on compliant substrates represents a classic problem in mechanics. Tremendous theoretical and experimental studies (Audoly and Boudaoud, 2008; Cai et al., 2011; Cao et al., 2012; Chen and Hutchinson, 2004; Efimenko et al., 2005; Groenewold, 2001; Harrison et al., 2004; Huang, 2005; Huang and Im, 2006; Huang and Suo, 2002; Huang et al., 2006; Huang et al., 2005; Jiang et al., 2007; Li et al., 2012; Liu et al., 2019; Ma et al., 2016b; Mei et al., 2011; Stafford et al., 2004; Sun et al., 2011; Wang et al., 2016; Wu et al., 2017; Xu et al., 2015a; Xu et al., 2014) of this instability mechanics have been carried out, over the last several decades. The duality of buckling/ instability suggests that this phenomenon can be controlled to derive delicate structures with desirable surface morphologies and geometric/ spatial dimensions. These investigations create renewed interest in this area that persists today, with many active research groups currently exploring basic scientific aspects (Jiang et al., 2007).

In addition to the abovementioned design paradigms, alternatives rely on mechanics design in the substrate and in variable geometrical material structures with strain limit (Bai et al., 2020; Fan et al., 2020; Holmes, 2019; Ma et al., 2016a; Yan et al., 2019; Zhang et al., 2015b) represent key points of uniqueness in developing the pluripotent flexible materials and devices. The promising design strategy of strain-limiting wrinkled kirigami with different geometries is inspired by the Japanese art of paper folding and cutting, kirigami. Corresponding to the second design paradigm involving flexible bilayer systems, the instabilities occur when compliant substrate has the finite thickness. Intuitively, one would believe that if the compliant substrate is thin enough the whole system can be in a state with global buckling and local wrinkling. Naturally, one wonders when the critical transition occurs. Such an issue together with other related ones, such as the interaction between built-in geometries and applied loading, will be demonstrated in current research using tension experiments, numerical calculations, plane-strain beam theory, energy approach, finite deformation theory and stability analysis. As far as the authors are aware of, the effect of such a finiteness on the buckling physics of strain-limiting wrinkled kirigami has not been examined. The only closely related study focused on strain-limiting substrate material in which the bilinear stress–strain behavior can be introduced to realize the low effective modulus and ability to accommodate large strain deformations with elastic response (Ma et al., 2016a). Little work has been done on the problem of the mechanics performance of the strain-limiting wrinkled kirigami material, and this is especially true for the cases of coexistent high flexibility, stretchability and compressibility. Also, the microstructural geometry and material property effects on the nonlinear mechanics responses are rarely investigated as well, which require an underpinning mechanics theory to guide the design in practical applications.

This paper is organized as follows. Section 2 illustrates the design strategy of strain-limiting wrinkled kirigami material, and describes the analytical models of normalized flexibility, stretchability and compressibility using plane strain theory, energy approach, buckling theory regarding finite deformations and geometric nonlinearities. Section 3 summarizes the numerical and experimental methods, and presents the parameterization analysis of the underlying relationships between dimensionless parameters and nonlinear responses associated with normalized flexibility, stretchability and compressibility. Accuracy

verification of developed models is also demonstrated using numerical calculations and in-situ tensile experiments in this section. Section 4 gives the concluding remarks.

2. Design strategy and analytical model

The strain-limiting wrinkled kirigami material (i.e., the kirigami material with highly parallel global buckling and local wrinkling effects due to strain limit) we demonstrated in current research is established by considering one-directional periodic boundary condition (see panel ⑤ in Fig. 1, for details). The schematic illustration in Fig. 1 presents the fabrication process. To highlight our design paradigm, a typical unit cell can be refined. The first step in fabrication involved patterning a compliant substrate using the designed mould with kirigami geometry (i.e., a cube mould with an embedded thin plate, see the small gap in panel ①. Here, the small gaps can guarantee the connectivity of a compliant kirigami substrate). Next, the compliant kirigami substrate (such as PDMS or acrylic dielectric elastomer substrates) can be formed by casting (~70℃, ~4 h) and thermally curing a mixture (such as the weight of 10:1) of base resin to crosslinking agent (Carpi et al., 2010; Jiang et al., 2007). And then, a compliant kirigami substrate with the initial length l_0 and finite thickness $2H$ is first stretched to produce a prestrain ε_p (see panel ③ in Fig. 1, the corresponding length: $l_1 = l_0(1 + \varepsilon_p)$). Two stiff thin films with the thickness of h are separately bonded onto the upper and lower surfaces of finite thickness substrate with prestrain. When the prestrain of substrate is released, the global buckling due to finite thickness effect of substrate and local wrinkling (described by the mean wavelength λ and amplitude A) from thin film surface occur (see panel ④ in Fig. 1). Therefore, the essence of our design is that after forming highly parallel global buckling and local wrinkling we have a strain-limiting wrinkled kirigami with built-in curvature and wrinkles, with the delicate variation of interaction between built-in geometries and applied loading, the resultant kirigami material can cause the high normalized flexibility, stretchability as well as compressibility.

Concretely speaking, at small applied strain, such material has the high flexibility, and the de-bending effect can guarantee the outstanding flexibility. To provide insights into built-in geometry-dependent mechanics responses associated with large substrate curvature. The analytical models with respect to plane-strain composite beam theory and large-curvature curved beam (LCCB) theory are established to determine the theoretical results for normalized flexibility (see SI Appendix Note 1, for details). Symmetry as the simplified measure is applied, and one quarter of the strain-limiting wrinkled kirigami unit cell is determined. Next, this simplified process of the analytical model is performed by clamping its left end. Correspondingly, the right end (see Fig. A2 in Note 1, for details) undergoes a balancing force F and a balancing moment M_0. Based on dimensional analysis method, the following dimensionless parameters can define the proposed kirigami material, i.e., the initial length/ substrate thickness l_0/H and the ratio of film and substrate thickness h/H (as well as the total thickness$(h + H)/$ substrate thickness $H_k/H = h/H + 1$, see LCCB theory in Note 1, for details). And then, a series of strain-limiting wrinkled kirigami can be designed by different combinations of these dimensionless parameters.

Close-form theoretical solutions with respect to normalized flexibility are derived by considering the plane-strain composite beam theory and large-curvature curved beam (LCCB) theory as detailed in Section 1 and Section 2 of SI Appendix Note 1, respectively. In particular, the analytical solution regarding composite beam theory is available for small width/radius ratio, such as < 0.2 (see Section 2.1 in SI Appendix Note1, for details). The first key mechanics index regarding the normalized flexibility $\bar{f}_{fle}$ using LCCB theory (i.e., the effective flexibility δ_x/F of the strain-limiting wrinkled kirigami normalized by that of a defect-free straight ribbon $l_0/A_{11}H_k$ of the same end-to-end length in the unit cell (Wang et al., 2020).), can be calculated by
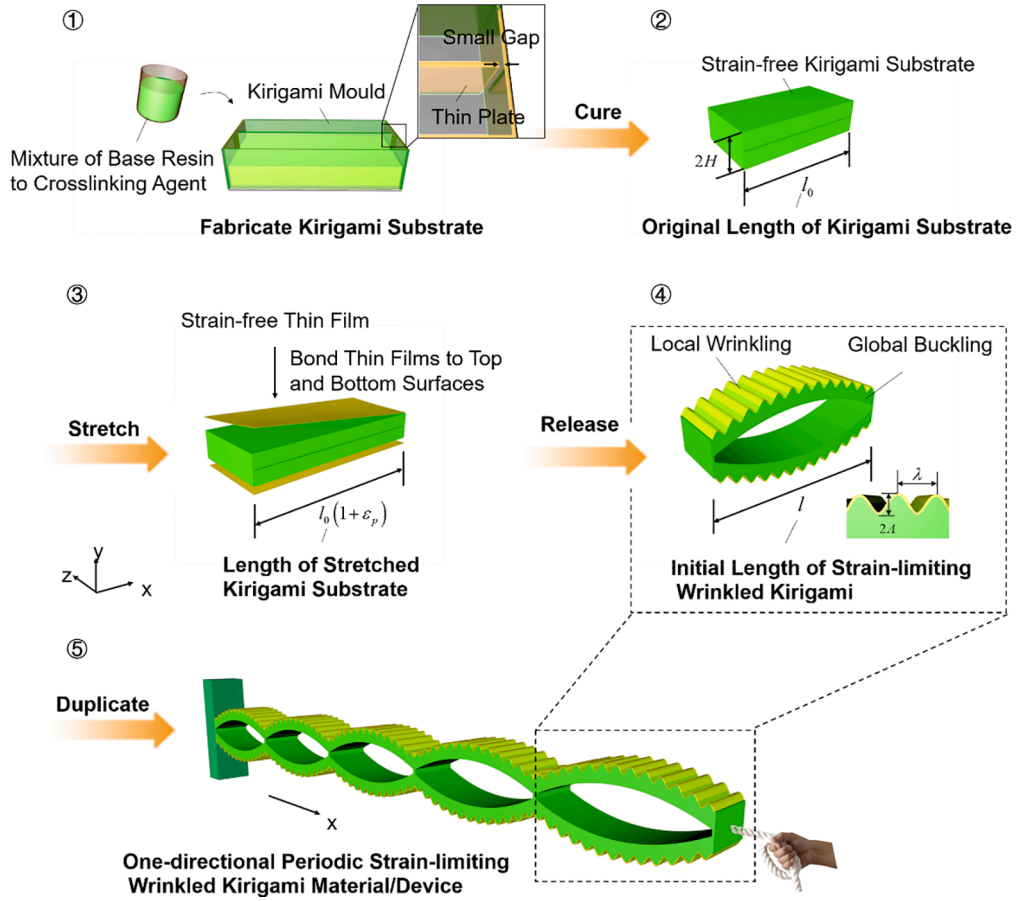
Fig. 1. Schematic illustration of the process for fabrication of strain-limiting wrinkled kirigami material/device.

$$\bar{f}_{fle} = \delta_x A_{11} H_k / F l_0 = \delta_x A_{11} (h + H) / F l_0 \tag{1}$$

where A_{11} is designated as the equivalent modulus of strain-limiting wrinkled kirigami to simplify the problem, as the high flexibility can be strongly influenced by the de-bending effect. Moreover, it is found that A_{11} is an intermediate quantity (i.e., the normalized flexibility $\bar{f}_{fle}$ is not related to the equivalent modulus A_{11}). δ_x is the horizontal displacement corresponding to applied loading.

Since the analytical model in Fig. A2 (see SI Appendix Note1, for details) is a statically indeterminate problem, the balancing moment should be determined firstly. In SI Appendix Note 1, applying energy principles and variational methods gives the following relation for achieving the unknown M_0

$$M_0 = FR(\theta_k - 2sin(\theta_k/2) + 2Jsin(\theta_k/2))/\theta_k \tag{2}$$

where R is the curvature radius, $\rho = 1/R$ is the corresponding curvature, $0 < \theta_k < \pi$ is the central angle, and $J = 1 - (H_k/R)/ln\,((2 + H_k/R)/(2 - H_k/R))$ represents the effect of large-curvature curved beam (i.e., the pure bending normal stress of the curved beam exhibits a hyperbolic variation along its cross section). Through Eqs. (1) and (2), the $\bar{f}_{fle}$ associated with dimensionless parameters $(h/H, l_0/H, \bar{E}_f/\bar{E}_s)$ can be given using the following equation:

$$\bar{f}_{fle} = \bar{f}_{fle}(h/H, l_0/H, \bar{E}_f/\bar{E}_s) \tag{3}$$

where $\bar{E}_f = E_f/\left(1 - \nu_f^2\right)$ and $\bar{E}_s = E_s/\left(1 - \nu_s^2\right)$ are plane strain modulus of the thin film and substrate, respectively. ν_f and ν_s are the corresponding Poisson's ratios. The explicit form of Eq. (3) is given in SI Appendix Note 1: see Eq (A26). We should note that the close-form

solution regarding Eq (A18) in SI Appendix Note 1 is derived based on the conventional composite beam theory.

The second key mechanics index is the normalized stretchability. Three typical deformation effects, including de-bending effect (the limitation conditions are provided in SI Appendix Note 4), de-wrinkle effect and de-prestrain effect, can result in the significant stretchability of strain-limiting wrinkled kirigami. As evident from Fig. 2, the strain-limiting wrinkled kirigami removes the built-in curvature to recover its flat configuration in the first stage (horizontal length: l to l_2). And the thin film is still in its wrinkled state. With the increment of applied loading, de-wrinkle occurs for wrinkling surface of material. Due to flattering process of wrinkles, the horizontal length of the system changes from l_2 to l_3 in the second stage of de-wrinkle. After previous two stages, the system becomes fully flat, however, the residual prestrain and critical buckling strain remain. Therefore, the variation in horizontal length because of de-prestrain effect can be calculated by $l_3\varepsilon_0$, where $\varepsilon_0 = \left(3\bar{E}_s/\bar{E}_f\right)^{2/3}/4$ represents the critical buckling strain (or the minimum strain to induce the wrinkling/buckling, see Eq. (B26) in SI Appendix Note 2, for details). Next, with the ending of de-prestrain stage, further enhancement of applied loading can lead to the intrinsic rapture of thin film. In SI Appendix Note 5, assumption associated with constant contour length gives the following relationship for obtaining the horizontal length l_3:

$$\lambda l_3 = l_2 \int_0^\lambda \sqrt{1 + (w')^2}dx = l_2 \int_0^\lambda \sqrt{1 + (Aksin(kx))^2}dx \tag{4}$$

where $w = Acoskx$ is the out-of-plane displacement for the thin film, $k = 2\pi/\lambda$, λ and A are wavelength and amplitude of wrinkle, respectively.

For the derivation of theoretical solution regarding normalized stretchability (see SI Appendix Note 5, for details), we adopt the buck-
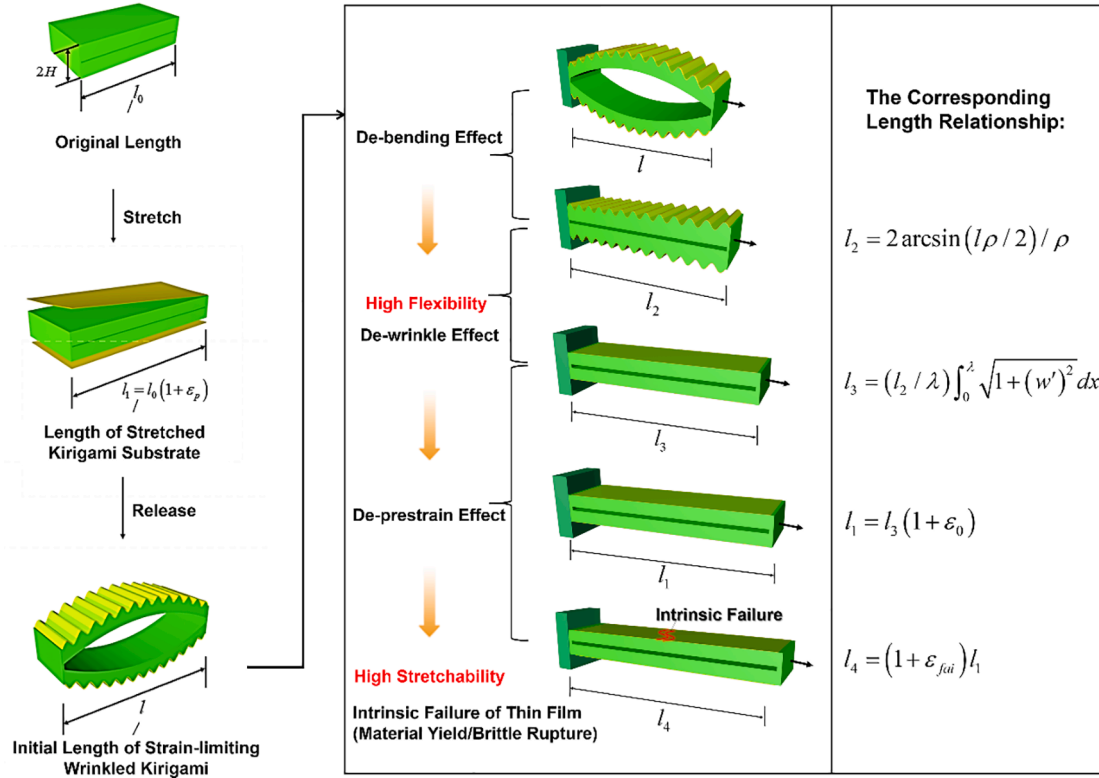
Fig. 2. Schematic illustration of deformation evolutions for the strain-limiting wrinkled kirigami material under stretching. Three typical effects including de-bending effect, de-wrinkle effect and de-prestrain can guarantee the high stretchability (high flexibility can be strongly influenced by the de-bending effect).

ling theory associated with finite deformations and geometric non-linearities (see SI Appendix Note 3, for details) to produce the quantitatively description of the wavelength λ and amplitude A:

$$\lambda = \lambda_* \lambda_0 / \left((1 + \varepsilon_p) \sqrt[3]{1+\xi} \right) \tag{5}$$

$$A = A_* A_0 / \left(\sqrt{1+\varepsilon_p} \sqrt[3]{1+\xi} \right) \tag{6}$$

where $\xi = 5\varepsilon_p (1+\varepsilon_p)/32$. $\lambda_0 = 2\pi h \sqrt[3]{\overline{E}_f/(3\overline{E}_s)}$ and $A_0 = h\sqrt{\varepsilon_p/\varepsilon_0 - 1}$ are the wavelength and amplitude based on small deformation theory. λ_* and A_* are prefactors, and ε_p is defined as the prestrain. As the classical column buckling characterizations with respect to wavelength and amplitude are not suitable for such a highly nonlinear problem (see SI Appendix Note 2 to Note 5, for details). Next, combining the evolutions of horizontal lengths (i.e., l, l_2, l_3, l_1 to l_4), the normalized stretchability of strain-limiting wrinkled kirigami material can be defined as

$$\overline{\varepsilon}_{str} = \left((1 + \varepsilon_{fai})(1 + \varepsilon_p) l_0 - l \right) / l \varepsilon_{fai} \tag{7}$$

where ε_{fai} is the intrinsic failure strain of the thin film. According to Eqs. (4) to (7), SI Appendix Note 5 gives the following relationship for normalized stretchability associated with dimensionless parameters $\left(h/H, l_0/H, \overline{E}_f/\overline{E}_s, \varepsilon_p, \varepsilon_{fai}, \lambda_* \right)$, i.e.,

$$\overline{\varepsilon}_{str} = \overline{\varepsilon}_{str} \left(h/H, l_0/H, \overline{E}_f/\overline{E}_s, \varepsilon_p, \varepsilon_{fai}, \lambda_* \right) \tag{8}$$

where the explicit form of Eq. (8) is provided in SI Appendix Note 5: see Eqs. (D7) to (D9).

The third important mechanics index is the normalized compressibility. As can be seen from Fig. E1 (see SI Appendix Section E, for details), an analytical model can be established to achieve the normalized compressibility for strain-limiting wrinkled kirigami. The top section in a unit cell can be refined based on the symmetry consideration. A

compressive force F (x-direction) is applied at the right end of the analytical model. The peak strain ε_m (i.e., film strain) can be determined according to the film thickness and curvature radii of film/substrate system at the extrema of the waves. And based on the finite deformation theory and assumption of constant contour length (see SI Appendix Note 3 and Note 6, for details), the peak strain can be calculated using the following relation:

$$\varepsilon_m = \varepsilon_{ms} + \varepsilon_{mf} \tag{9}$$

$$\varepsilon_{ms} = h\rho_s/2 = \varepsilon_{ms}\left(h/H, \overline{E}_f/\overline{E}_s, \varepsilon_p \right) \tag{10}$$

$$\varepsilon_{mf} = h\rho_f/2 = \varepsilon_{mf}\left(\overline{E}_f/\overline{E}_s, \varepsilon_p, \varepsilon_{app} \right) \tag{11}$$

where ε_{app} is defined as the applied strain, ρ_s represents the substrate curvature, ρ_f represents the curvature at peak or trough of the thin film. And the details with respect to Eq. (9) to Eq. (11) are provided in SI Appendix Note 6.: see Eqs. (E4)-(E5). Next, the key mechanics index towards the normalized compressibility is defined using a continued equality, i.e.,

$$\overline{\varepsilon}_{com} = \varepsilon_{com}/\varepsilon_{fai} = \varepsilon_{app}/\varepsilon_m \tag{12}$$

where ε_{com} represents the elastic compressibility. The failure criterion we adopted here is $\varepsilon_m = \varepsilon_{fai}$. For example, ε_{fai} is the corresponding yield strain for the typical elastic–plastic materials. Finally, the normalized compressibility based on Eq. (12) can be related to dimensionless parameters $\left(h/H, \overline{E}_f/\overline{E}_s, \varepsilon_p, \varepsilon_{fai} \right)$ by

$$\overline{\varepsilon}_{com} = \overline{\varepsilon}_{com}\left(h/H, \overline{E}_f/\overline{E}_s, \varepsilon_p, \varepsilon_{fai} \right) \tag{13}$$

where the explicit form of Eq. (13) is provided in SI Appendix Note 6: see Eqs. (E7).

So far, key mechanics indexes associated with normalized flexibility, stretchability and compressibility have been determined. Preliminary

inspiration of Eqs. (3), (8) and (13) indicates that it is difficult to ascertain the evolutional relations between normalized mechanics indexes and dimensionless parameters due to the complexity of theoretical solutions. And thus, further analysis should be suitably performed to uncover the underlying relations of three key indexes and various dimensionless parameters, as we provided in Section 3. In addition, to provide a full understanding of highly parallel global buckling and local wrinkling, the limitation conditions, including the critical prestrain and the critical length, are provided in SI Appendix Note 4. According to theoretical solutions, numerical calculations and experimental results, the corresponding investigations are also carried out in Section 3.

3. Results and discussion

3.1. Comparison of theoretical, computational and experimental results

In current research, all numerical simulations are performed with use of nonlinear, plane strain finite element method (FEM) in the ABAQUS commercial software. The compliant substrate is modeled using dielectric elastomer with Young's modulus of 0.18 MPa and Poisson ratio of 0.45. The stiff film is designated as polyimide (PI) thin film with Young's modulus of 2.5 GPa, Poisson ratio of 0.34 and yield strain of 0.02. To induce the global buckling and local wrinkling, initial geometry imperfection from linear perturbation is introduced to update the
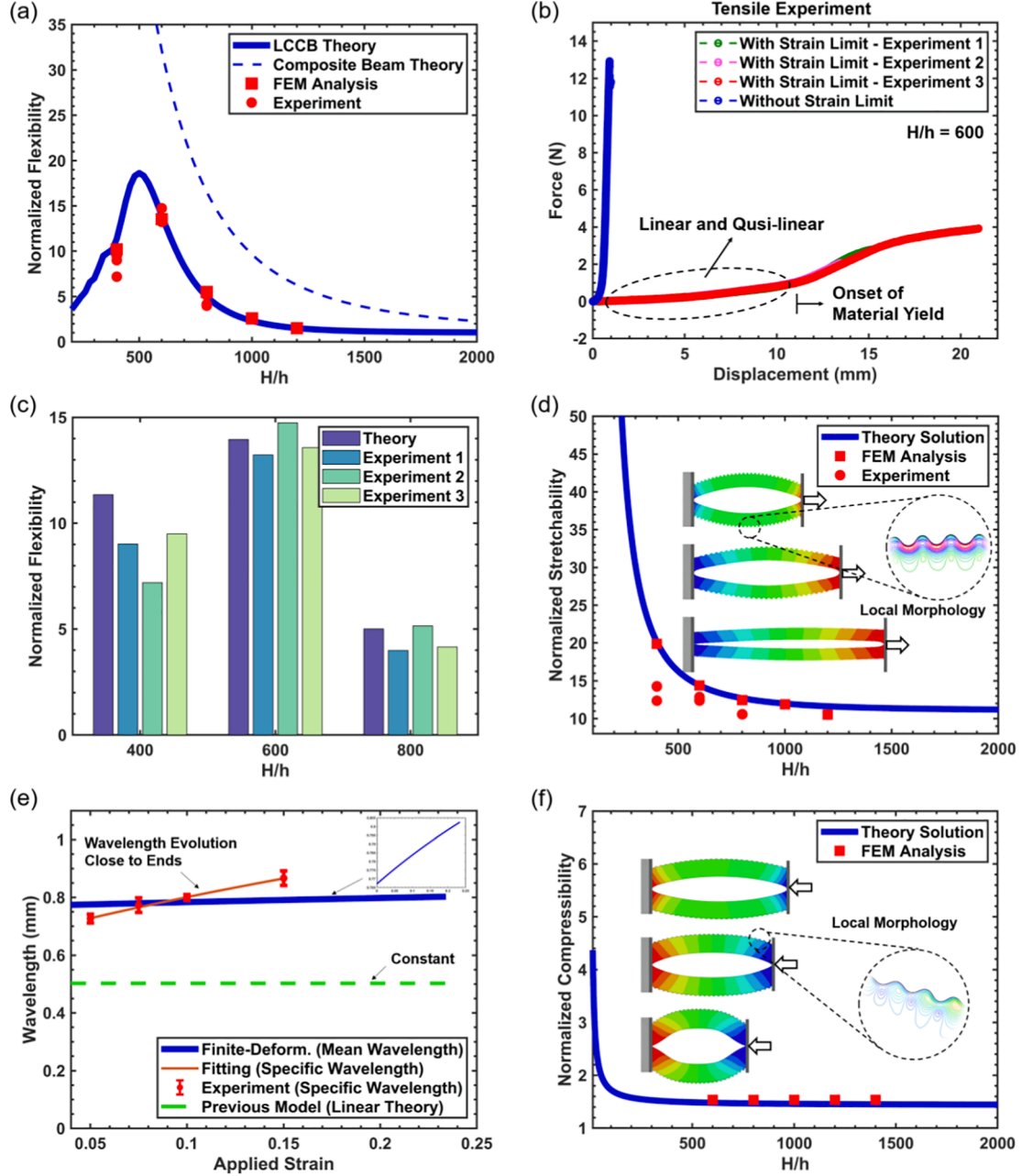

Fig. 3. Comparison of theoretical, numerical and experimental results for normalized flexibility, stretchability and compressibility. (a) Normalized flexibility versus substrate-to-film thickness ratio based on theoretical solution and FEM results. (b) Experimental force–displacement curves for the representative strain-limiting wrinkled kirigami materials. (c) Normalized flexibility versus substrate-to-film thickness ratio based on theoretical results and experiments. (d) Normalized stretchability versus substrate-to-film thickness ratio based on theoretical solutions and FEM calculations. (e) Wavelength of buckled strain-limiting wrinkled kirigami of thin film on substrate as a function of the applied strain. The finite-deformation buckling theory yields wavelengths that can agree well with experiments. (f) Normalized compressibility versus substrate-to-film thickness ratio based on theoretical solutions and numerical calculations.

computational model. The equivalent deformation associated with pre-strained substrate is introduced by initial predefined field. And then, the size of elements is carefully determined using convergence test.

The tensile experiment based on high-precision in-situ tensile system (including CMOS connected to the computer, optical microscope, and miniature tester, see Fig. 4c for details) is performed to validate the analytical model. For the strain-limiting wrinkling kirigami material, the sample is carefully clamped with skidproof chunks of the in-situ tester. The slow tension velocity of 0.0005 m/s is carried out to obtain the micromesh force–displacement curve. Based on Eq. (1), one can separately determine the elongation in the strain-limiting wrinkle kirigami and in a defect-free (without curvature and wrinkling) film/substrate system. For specific geometries, the experiments are determined using a number of kirigami materials, and optical microscope (see Fig. 4c for details) can be used to characterize the local morphology of strain-limiting wrinkling kirigami. As evident from Fig. 4a, Fig. 4d and Fig. 4e, experimental snapshots of postbuckling process with regard to strain-limiting wrinkled kirigami material are provided, the typical de-bending, de-wrinkle, de-prestrain phenomena can be observed during the tension tests.

Figure 3a shows the typical evolution of normalized flexibility with the increasing thickness ratio H/h for strain-limiting wrinkled kirigami: first a monotonic increase of $\bar{f}_{fle}$ followed by a drop, after which the normalized flexibility varies in a lesser extent. The results from FEM agree well with the LCCB theoretical analysis, while the analytical solution with respect to composite beam theory in Fig. 3a is only available for small width/radius ratio (see SI Appendix Note 1 and Note 2, for details). Here, the prestrain and initial length must be larger than the transitions because of the finite thickness effect of compliant substrate (see SI Appendix Note 4, for details). Fig. 3b and Fig. 3c provide comparison of LCCB theoretical solutions obtained from Eq. (3) and experimental results corresponding to different thickness ratios ($H/h = 400$, 600, 800). For all samples in experiments, the large width in z-direction (see Fig. 1, for details) is applied to model the plane strain state and suppress the lateral buckling. The force–displacement curves in Fig. 3b obviously show that the strain-limiting wrinkled kirigami ($H/h = 600$) is always more compliant (see the slope of $\bar{f}_{fle}$) than that of defect-free (i. e., without strain limit) film/substrate system due to de-bending effect. Normalized flexibility for experimental samples in Fig. 3c is in surprisingly good agreement with the theoretical prediction, indicating the theoretical model considering LCCB theory and energy approach can be effective to provide insights into the design of strain-limiting wrinkled kirigami.

Figure 3d shows the nonlinear relation between normalized stretchability $\bar{\varepsilon}_{str}$ based on Eq. (8) and substrate-to-film thickness ratio H/h for the strain-limiting wrinkled kirigami. The analytical solution and numerical results are separately plotted as the black dash line and red filled rectangles. The evolution of $\bar{\varepsilon}_{str}$ is monotonic. With increasing of H/h the normalized stretchability decreases, suggesting that the large substrate-to-film thickness ratio, in principle, is always detrimental to the enhancement of stretchability. Particularly, in the case of $H/h = 400$, the normalized stretchability is equal to 20.14, indicating that the stretchability is increased by 20.14 times as compared with that of the single system consisting of thin film material without strain-limiting design (i.e., without global buckling and local wrinkling). As shown in Fig. 3e, the average amplitude given in Eq. (6) expression (i.e., theoretical results) agrees well with the experimental results (see Fig. 4d, for details), while the amplitude A_0 based on the previous linear theory (see SI Appendix Note 2, for details) clearly underestimates.

Figure 3f displays the dependency between normalized compressibility $\bar{\varepsilon}_{com}$ from Eq. (13) and substrate-to-film thickness ratio H/h. With increasing of H/h the normalized compressibility is monotonic decreasing, where the black dash line and red filled rectangles represent the solution for $\bar{\varepsilon}_{com}$ and FEM results, respectively. Here, insensitive evolution of normalized compressibility presents the relatively low and stable enhancement of compressibility. However, the comprehensive understanding stemmed from parameterized designs can give us the broader landscapes regarding normalized compressibility. Over the whole domain from Fig. 3d and Fig. 3f, the FEM results are in excellent agreement with the analytical solutions.

Figure 4a and b show the head-to-head comparison of experimental and numerical postbuckling deformation evolution for strain-limiting wrinkled kirigami with $H/h = 600$, associated with the significant de-bending, de-wrinkle and de-prestrain effects for the applied strain from 0 to 27.7%. The amplitude and wavelength of wrinkles are decreasing (down to zero) and increasing (up to ∞) with the increasing of applied strain, respectively, which agree with the analysis based on finite-deformation buckling theory. To provide a clearly comparison, the color bars in corresponding numerical calculations ($H/h = 600$ for Fig. 4b) represent the principal strains. And the postbuckling deformations from FEM calculations are consistent with experimental images. In Fig. 4c to 4e, optical images of local (close to ends of strain-limiting wrinkled kirigami, see Fig. 4d for details) and global (see Fig. 4e for details) buckling morphologies are provided. As we can see from the snapshots in Fig. 4d and Fig. 4e ($H/h = 800$), the strain-limiting wrinkled kirigami materials undergo the combined de-bending and de-wrinkle deformation. With increasing of applied strain, the specific wavelength increases, as evident from Fig. 4d. According to the discrete Fourier spectrum-based inversion (Hou et al., 2021), the wrinkling amplitude can be evaluated using $A = 2\lambda\sqrt{l_w/\lambda - 1}/\pi \approx 2\lambda\sqrt{1/\sqrt{1 - \pi^2 h^2/6\lambda^2} - 1}/\pi$, which is a typical monotone decreasing function with the increasing of wrinkling wave-length and specific thickness of h. In particular, if $\lambda = l_w$ (l_w represents the cross-sectional half arc-length of a single wrinkle wave), the wrinkling amplitude is equal to zero (see applied strain of 0.268 in Fig. 4d, for details).

Moreover, Fig. D1 (see SI Appendix Note5, for details) shows the mean wavelength of the surface wrinkles in our experiments, which can agree well with the evaluation based on Eq. (5) when λ_* is equal to 2. This comparison also suggests a non-negligible change of wavelength and amplitude between the wrinkles with and without built-in curvature because of strain-limiting effect.

Figure 4f indicates that strain-limiting wrinkled kirigami materials can offer coexistent high flexibility, stretchability and compressibility, and our design strategies can be suitable for both discrete and distributed flexible systems, enabling strain-limiting wrinkled kirigami to accommodate extreme mechanical deformations without damage, such as stretching, compressing and twisting like a rubber ribbon. Finally, we find that the robustness of the strain-limiting wrinkled kirigami with conductive polymer-silver film can be demonstrated by the stable brightness of light emitting diode under the high stretching, compressing and twisting, opening up the tremendous possibility for many device applications (see Fig. 4g). Especially, the large stretching strains enabled by strain-limiting wrinkled kirigami with conductive polymer film may have the increasing resistance (see Fig. 4h), potentially useful in a variety of devices, including stretchable current collectors, electrodes and piezoelectric harvesters (Shyu et al., 2015). However, such a large resistance change might not be acceptable in some practical applications. Further work should be directed at studying how stable resistance curves could be generated using the strain-limiting wrinkled kirigami with an extremely large applied strain. For the present analysis, it has been found that these normalized resistances remain almost unchanged during the linear response and quasilinear response stages (see Fig. 3b and Fig. 4h, for details). To evaluate and check the stability and reliability, the load-applied strain curves of strain-limiting wrinkled kirigami are provided in Fig. 4i. Generally, the curves at cycle 40 can match well with the curves at cycle 1, implying small strain energy losses.
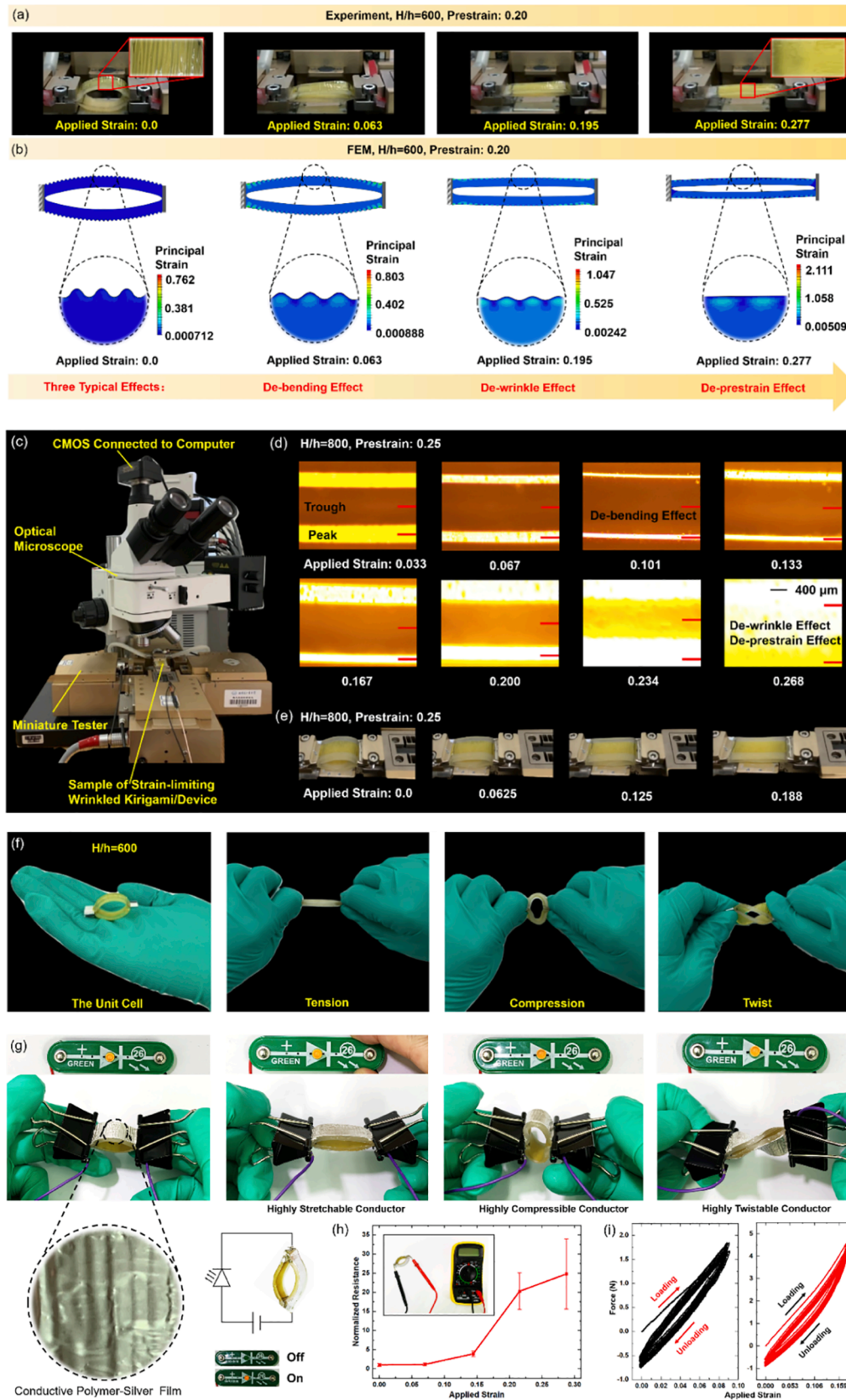
Fig. 4. (a-b) The head-to-head comparison of postbuckling deformation evolution for strain-limiting wrinkled kirigami with $H/h = 600$ among experiments and FEM results. The significant de-bending, de-wrinkle and de-prestrain phenomena can be detected during the experimental observation and corresponding simulation snapshots, where the color bars represent the strains. (c) Experimental apparatus for measuring the force–displacement curves and detailed wrinkle morphologies. (d) Optical micrographs of buckled strain-limiting wrinkled kirigami ($H/h = 800$), formed with various applied strain. The wavelength increases and amplitude decreases systematically as the applied strain increases (see Supplementary Movie). (e) Postbuckling deformation evolution for strain-limiting wrinkled kirigami with $H/h = 800$. (f) Optical image of a freely deformed strain-limiting wrinkled kirigami, which can accommodate extreme mechanical deformations without damage, such as stretching, compressing and twisting like a rubber ribbon. (g) Schematic illustration and demonstration of the strain-limiting wrinkled kirigami with conductive polymer film can be highly stretchable, compressible and twistable as an electrical conductor to wire light emitting diode. (h) Variations in normalized resistance of the strain-limiting wrinkled kirigami with conductive polymer film under different strain conditions. (i) The load-applied strain curves of strain-limiting wrinkled kirigami, implying small strain energy losses for 40 cycles of loadings.

3.2. Parameterization analysis of strain-limiting wrinkled kirigami

In this section, we perform the parameterization analysis and unveil the effects of typical dimensionless parameters from Eqs. (3), (8) and (13) on the normalized flexibility, stretchability and compressibility. Limitation conditions involving highly parallel global buckling and local wrinkling of strain-limiting wrinkled kirigami are also demonstrated. We anticipate the collective results can provide the comprehensive understanding and reliable guideline in enhancing flexibility, stretchability and compressibility for novel strain-limiting wrinkled kirigami materials.

3.2.1. Effects of geometry parameters on normalized flexibility

Figure 5a and b respectively show the effects of substrate-to-film thickness ratio H/h and film-to-substrate modulus ratio $\overline{E}_f/\overline{E}_s$ on normalized flexibility with various initial length l_0 (or l_0/H). Obviously, Fig. 5a presents that with increasing of H/h for specific initial length/substrate thickness ratio l_0/H the normalized flexibility is non-monotonic: when H/h is closed to the maxima, it causes a drastic drop of $\overline{f}_{fle}$. For specific thickness ratio, however, the larger initial length will lead to the significant enhancement regarding $\overline{f}_{fle}$. For example, normalized flexibility with large l_0/H is increased by 573.09 times as compared with that of small l_0/H (see red dots in Fig. 5a from the parameters $(H/h, l_0) = (2800, 16mm)$ to $(H/h, l_0) = (2800, 866mm)$). This also constitutes dramatic evidence of ultra-high flexibility for strain-limiting wrinkled kirigami, which is reasonably robust than that of strain-limiting substrate materials without built-in curvature for stretchable and flexible electronics (Ma et al., 2016a). Fig. 5b reveals the typical evolutions for the increasing of film-to-substrate modulus ratio $\overline{E}_f/\overline{E}_s$: first a linear increase of $\overline{f}_{fle}$, and then followed by a moderate drop, for the specific initial length/substrate thickness ratio. When $\overline{E}_f/\overline{E}_s$ is constant, however, with the increasing of l_0/H the normalized flexibility increases except for some unanticipated expectations, as evident from elliptical frame in Fig. 5b. Based on these findings associated with different dimensionless parameters (i.e., H/h, l_0/H and $\overline{E}_f/\overline{E}_s$), we find that remarkable initial length design can, in some case, carry tremendous potential in enhancing the flexibility. And for biomedical device applications, the high flexibility can match the values (such as $1 < \overline{f}_{fle} < 580$ in Fig. 5a and Fig. 5b) beyond those of targeted biological tissues, avoiding any mechanical constraint on natural motions (Ma et al., 2016a).

Moreover, Timoshenko and Goodier (Timoshenko & Goodier, 1970; Wang and Wang, 2020; Wang et al., 2020) compared the elasticity theory with the LCCB theory and conventional beam theory for the pure bending of a beam with various width/radius ratio (rectangular cross-section). They found that LCCB solutions can be in good agreement with elastic solutions for a wide range of width/radius ratio ρ_{rel}. Here, the width/radius ratio can be determined using $\rho_{rel} = 6 \cdot 3^{2/3}(1 + h/H)\left(h^3\overline{E}_f/(H^3\overline{E}_s)\right)^{1/3}$ (see SI Appendix Note 2, for details), based on which Fig. A3 and Fig. A4 (see SI Appendix Note 2, for details) presents the evolution of ρ_{rel}. For the material parameters of $E_f = 2.5$GPa, $E_s = 0.18$MPa, $\nu_f = 0.34$ and $\nu_s = 0.45$ in Fig. A3 and the specific ratio of $H/h = 600$ in Fig. A4 (see SI Appendix Note 2, for details), the analytical solution with respect to conventional composite beam theory (see Eq. (A18) in SI Appendix Note1, for details) is only available for $\rho_{rel} < 0.2$, otherwise, the significant divergence can be obtained as we can see from Fig. 3a.

3.2.2. Effects of geometry parameters on normalized stretchability

To reveal the effects of dimensionless parameters on the normalized stretchability, we start by investigating the limitation conditions with regard to global buckling and local buckling of strain-limiting wrinkled kirigami. In SI Appendix Note 4, comparison of the potential energies $U_f + U_s$ and the total energy without wrinkle deformation $U_f' + U_s'$ suggests that global buckling and local wrinkling occur when $U_f' + U_s' > U_f + U_s$, and we have

$$\varepsilon_p > \left(1 + 4h\overline{E}_f/(H\overline{E}_s)\right)\left(k^2h^2/12 + g(kH)\overline{E}_s/(kh\overline{E}_f)\right) \tag{14a}$$

$$g(x) = \left(1 + 2x^2 + \cosh(2x)\right)/\left(-4x + 2\sinh(2x)\right) \tag{14b}$$

According to Eq. (14), Fig. 6a shows the critical prestrain ε_c curve for the increasing thickness ratio H/h. When $\varepsilon_p > \varepsilon_c$, the substrate cannot shrink to its initial length after the release of the prestrain, and the strain-limiting wrinkled kirigami with local/surface wrinkling will bend globally. Numerical calculations from FEM match well with the prediction in Eq. (14). While for the specific critical prestrain the material has a limit of the substrate-to-film thickness ratio (such as $(\overline{E}_f h^3)/(\overline{E}_s H^3) \approx 0.064$), below which global buckling (without wrinkling) occur. For the H/h above this limit, global buckling may still occur if the initial length l_0 above the critical length L_{cr} (see SI Appendix Note 4, for details). Fig. 6b presents the phase diagram regarding global buckling and local wrinkling for different dimensionless parameters L_{cr}/h and H/h. The inset shows the experimental image of global buckling kirigami material (PI thin film and dielectric elastomer substrate). It is hoped that applications of strain-limiting pluripotent materials in the flexible devices will become more frequent already in the near future, these limitation conditions have been considered in current research.

Figure 6c to f provide the distribution of normalized stretchability towards the dimensionless parameters, such as substrate-to-film
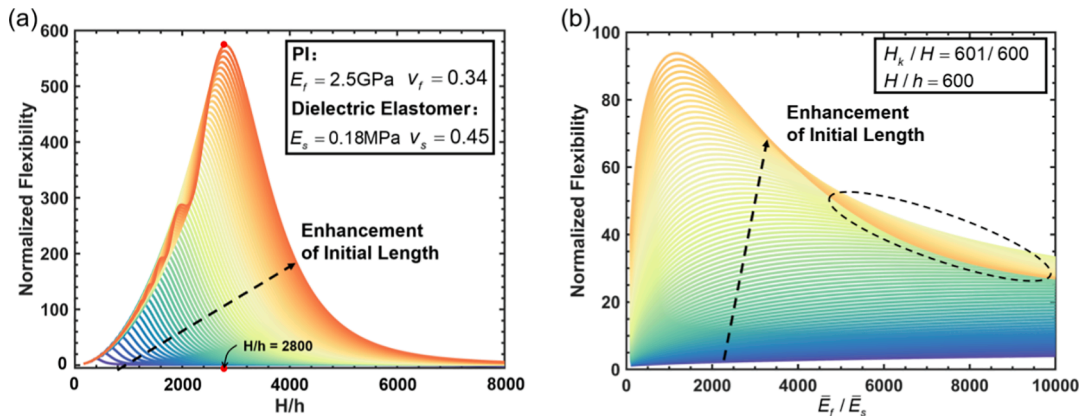

Fig. 5. (a) Distribution of the normalized flexibility for the thickness ratio H/h and initial length ($16mm \leqslant l_0 \leqslant 866mm$). (b) Distribution of the normalized flexibility for the film-to-substrate modulus ratio $\overline{E}_f/\overline{E}_s$ and initial length ($16mm \leqslant l_0 \leqslant 66mm$).
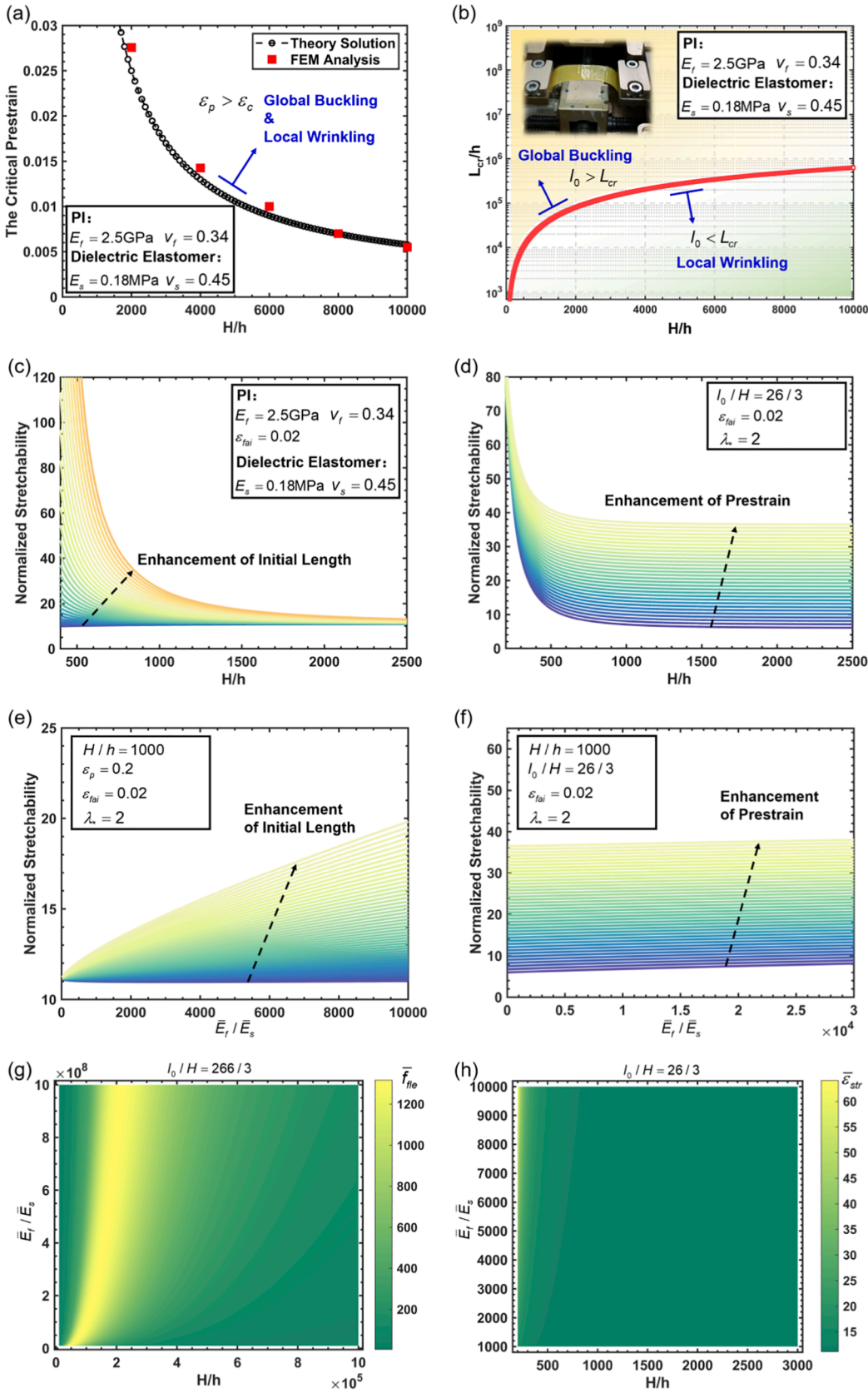
Fig. 6. (a) The critical prestrain versus substrate-to-film thickness ratio for a PI thin film on a dielectric elastomer. (b) The critical film length that separates local wrinkling from global buckling. (c) The effects of substrate-to-film thickness ratio on normalized stretchability for different initial lengths. (d) The effects of substrate-to-film thickness ratio on normalized stretchability for different prestrains. (e) The effects of film-to-substrate modulus ratio on normalized stretchability for different initial lengths. (f) The effects of film-to-substrate modulus ratio on normalized stretchability for various prestrains. (g) Distribution of normalized flexibility with regard to substrate-to-film thickness ratio and film-to-substrate modulus ratio. (h) Distribution of normalized stretchability with regard to substrate-to-film thickness ratio and film-to-substrate modulus ratio.

thickness ratio, initial length/substrate thickness ratio, prestrain and film-to-substrate modulus ratio. Fig. 6c shows the effects of H/h and l_0/H ($6mm \leqslant l_0 \leqslant 80mm$) on $\bar{\varepsilon}_{str}$. For the constant l_0/H, the larger thickness of the substrate will lead to convergent values of normalized stretchability. But so-called long arm effect associated with l_0 will significantly enhance the $\bar{\varepsilon}_{str}$, for the specific thickness ratio. Fig. 6d shows the evolutions of $\bar{\varepsilon}_{str}$ when $l_0/H = 26/3$, $\varepsilon_{fai} = 0.02$, $\lambda_* = 2$ and the prestrain varies ($0.1 \leqslant \varepsilon_p \leqslant 0.7$). For example, in the case of $\varepsilon_p = 0.7$ the normalized stretchability decreases with increasing of H/h. While, for a specific thickness ratio the $\bar{\varepsilon}_{str}$ increase linearly with the enhancement of prestrain for $H/h > 1000$. As can be seen from Fig. 6e and Fig. 6f, if we designate a constant thickness ratio, such as $H/h = 1000$, the effects of $\bar{E}_f/\bar{E}_s$ on normalized stretchability according to Eq. (8) can be directly demonstrated. Fig. 6e indicates that the large film-to-substrate modulus ratio and large initial length can bring substantial increases in the normalized stretchability. And the $\bar{\varepsilon}_{str}$ based on Eq. (8) is insensitive under the circumstance of a small ratio l_0/H, where initial length is from 16 mm to 66 mm. For the prestrain of 0.02 as illustrated in Fig. 6f, the normalized stretchability will increase slightly when $\bar{E}_f/\bar{E}_s$ changes from 0 to 30000. Equally, the $\bar{\varepsilon}_{str}$ increases linearly if the prestrain increases.

Up to now, parameterization analysis associated with normalized flexibility and stretchability by designating one design variable has been performed. Next, according to Eq. (3) and Eq. (8), Fig. 6g and Fig. 6h provide insights into the normalized flexibility and stretchability of strain-limiting wrinkled kirigami towards two typical design variables (i.e., the substrate-to-film thickness ratio H/h and film-to-substrate modulus ratio $\bar{E}_f/\bar{E}_s$). The color bars in Fig. 6g and Fig. 6h represent the values of $\bar{f}_{fle}$ and $\bar{\varepsilon}_{str}$, respectively. The most comprehensive understanding regarding Fig. 6g and Fig. 6h is that contour diagrams give us

not only the refined results (see Fig. 6h) to graphs in Fig. 6c to Fig. 6h but also the broader scopes of typical dimensionless parameters (see Fig. 6g).

3.2.3. Effects of geometry parameters on normalized compressibility

We have demonstrated that upon stretching strain-limiting wrinkled kirigami materials enable the high flexibility and stretchability due to de-bending, de-wrinkle and de-prestrain effects. There is, in fact, much evidence to indicate that the kirigami materials can bring increases in the compressibility, which develops the scope of practical applications. Fig. 7a to d show the parameterized investigations towards the peak strain and normalized compressibility. As according to Eq. (13) the normalized compressibility is found to be closely related to the peak strain. For the compression process of strain-limiting wrinkled kirigami, the peak strain will increase if the applied strain ε_{app} increases, as detailed in Fig. 7a. Equally, it can be seen from the plots that the enhancement of prestrain can cause the large peak strain based on Eqs. (9)-(11) (see SI Appendix Note 6, for details). For the different film-to-substrate modulus ratios, Fig. 7b shows the effects of $\bar{E}_f/\bar{E}_s$ on ε_m for the prestrain ranging from 0.1 to 0.9. With the increasing of $\bar{E}_f/\bar{E}_s$ and ε_p, the ε_m can decrease and increase, respectively. This contribution of dimensionless parametric properties on controllability associated with peak strain is accordance with previous experiments, such as those for single-crystal silicon on rubber substrates toward the high-performance electronics (Khang et al., 2006), which can signify the attractive ability for material design presents a promising technology in regulating (reducing or enhancing) the peak strain. Next, Fig. 7c and Fig. 7d provide the evolutions of normalized compressibility for H/h and $\bar{E}_f/\bar{E}_s$, separately. Fig. 7c reveals that the normalized compressibility $\bar{\varepsilon}_{com}$ will
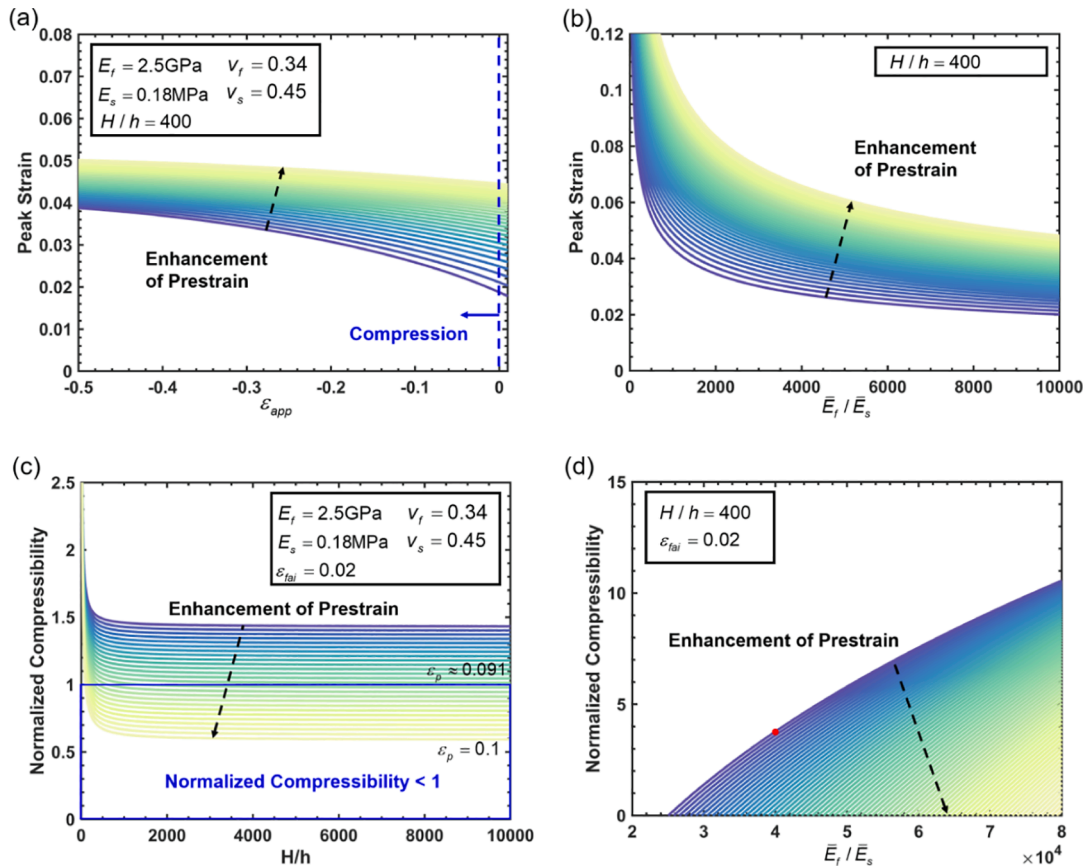

Fig. 7. (a) The peak strain verse applied strain with various prestrain. (b) The peak strain verse film-to-substrate modulus ratio with various prestrain. (c) The normalized compressibility evolutions for increasing prestrain and substrate-to-film thickness ratio. (d) The normalized compressibility evolutions for increasing prestrain and film-to-substrate modulus ratio.

decrease as the increasing of prestrain. And in some cases (i.e., $0.091 < \varepsilon_p < 0.1$) the $1/\bar{\varepsilon}_{com}$ will exceed 1, this suggests that the peak strain may exceed the applied strain according to Eq. (12). These observations directly demonstrate that compressibility design of strain-limiting wrinkled kirigami should be carefully performed, and not all the kirigami materials are helpful to increase the compressibility. Finally, Fig. 7d shows the enhancement of normalized compressibility by regulating the dimensionless parameters with respect to film-to-substrate modulus ratio and prestrain when $H/h = 400$ and $\varepsilon_{fai} = 0.02$. For example, in the case of $\bar{E}_f/\bar{E}_s = 40000$, such as PI thin film and ecoflex substrate with $\bar{E}_s = 60$kPa, the compressibility is increased by $\sim$ 4 times as compared with that of the single system consisted of thin film material without global buckling and local wrinkling (see red dot in Fig. 7d).

3.2.4. Compressibility of strain-limiting wrinkled kirigami based on stability analysis

Although the theoretical solution of normalized compressibility can provide the effective predictions and insights into rational design (see Fig. 7), there is always room for improvement. And much work should be devoted to a systematic investigation of geometric effects on compression-induced global buckling/instability and resultant compressibility, the authors will answer this question in this section. From the viewpoint of mechanics, the concept of geometric imperfection can be introduced to describe the strain-limiting effect of kirigami. Equally, the presence of the geometry imperfection can significantly affect their mechanical responses in the buckling process. Therefore, based on the moderate deformation assumption and analysis model obtained from experiments (see Fig. E1 in SI Appendix Note 7, for details), we investigate the compressibility of strain-limiting wrinkled

kirigami using the stability analysis (see SI Appendix Note 7, for details). Especially, a nonhomogeneous fourth-order ordinary-differential equation can be established to characterize the deformation state of strain-limiting wrinkled kirigami beam with geometric imperfection, i.e.,

$$\widehat{w}^{iv} + \widehat{F}\widehat{w}'' - \widehat{w}''\iota \int_0^1 \left(\widehat{w}^{2'} - \widehat{w}_0^{2'}\right)d\widehat{x}/2 = \widehat{w}_0^{iv} \tag{15}$$

where the prime represents the derivative of normalized deflection function with regard to the spatial coordinate $\times$, and the dimensionless parameters with respect to $\widehat{w}, \widehat{x}, \widehat{F}$ and ι are provided in Eq. (E14) (see SI Appendix Note 7, for details). Correspondingly, the critical buckling loading can be obtained using the following relation:

$$F_{critical} = -w_{mul}\pi^2\left(A_{axial}a_0^2 - 16D_{bending} - 12A_{axial}^{1/3}D_{bending}^{2/3}a_0^{2/3}\right)/4l^2 \tag{16}$$

where w_{mul} represents the width of kirigami beam (SI Appendix Note 1, for details), a_0 represents the midspan initial rise of wrinkled-kirigami beam (see Eq. (E19) in SI Appendix Note 7, for details), A_{axial} and $D_{bending}$ are the axial and bending stiffness (see Eq. (E12) in SI Appendix Note 7, for details), respectively. Moreover, based on the assumption of constant contour length, the minimum length l_{min} of strain-limiting wrinkled kirigami can be used to calculate the compressibility $\varepsilon_{com-stability} = (l - l_{min})/l$, i.e.,

$$\varepsilon_{com-stability} = \varepsilon_{com-stability}\left(h/H, l_0/H, \bar{E}_f/\bar{E}_s\right) \tag{17}$$

where l_{min} and l are provided in Eq. (E27) (see SI Appendix Note 7, for details) and Eq. (A17) (see SI Appendix Note 1, for details), respectively.

Figure 8a and b present the effects of substrate-to-film thickness ratio H/h and film-to-substrate modulus ratio $\bar{E}_f/\bar{E}_s$ on compressibility based
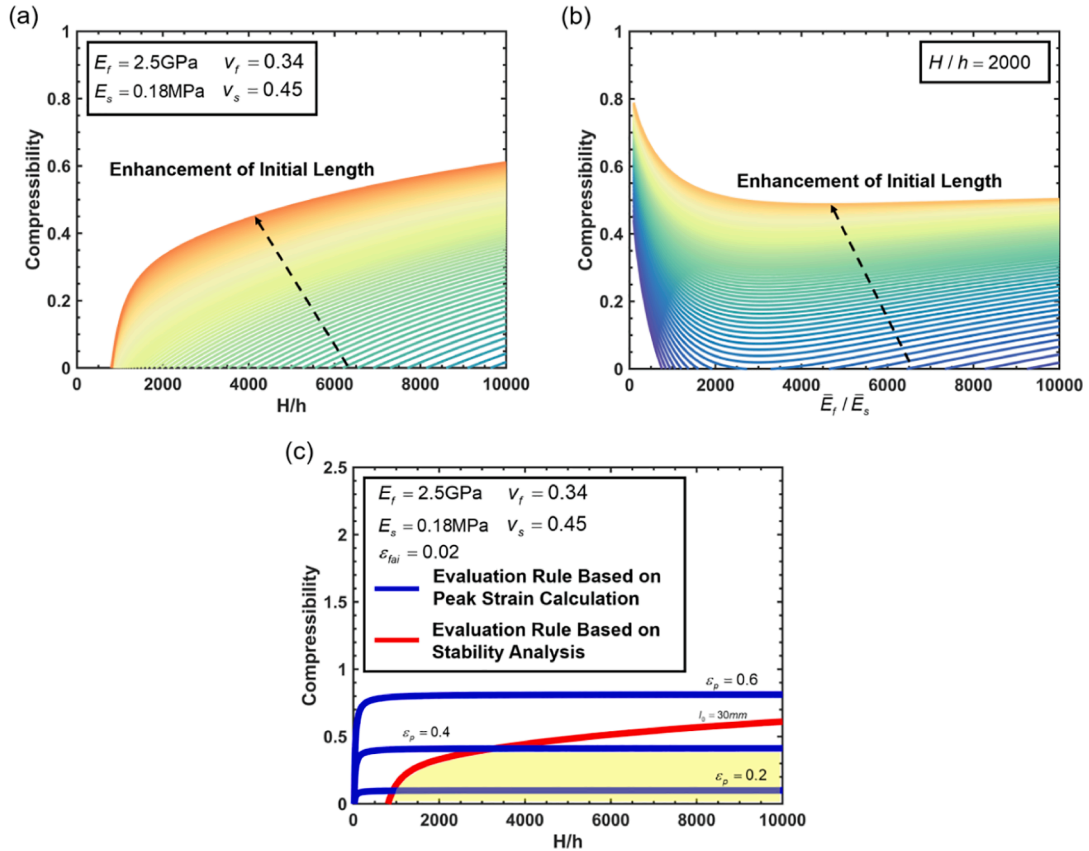

Fig. 8. (a) The effects of substrate-to-film thickness ratio on compressibility via stability analysis for various initial length. (b) Evolutions of compressibility based on stability analysis for increasing initial length and film-to-substrate modulus ratio. (c) Evolutions rules of compressibility with respect to peak strain calculation and stability analysis for different substrate-to-film thickness ratio.

on stability analysis with different initial length, i.e. l_0/H. With increasing of substrate-to-film thickness ratio H/h the compressibility is monotonic, as we can see from Fig. 8a. For a specific thickness ratio of H/h, the larger initial length ratio of l_0/H can lead to the larger compressibility. However, Fig. 8b shows that with increasing of film-to-substrate modulus ratio $\overline{E}_f/\overline{E}_s$ the compressibility $\varepsilon_{com-stability}$ based on stability analysis is nonmonotonic: first a significant decline of $\varepsilon_{com-stability}$ followed by a slight increase, after which the compressibility varies in a lesser extent. Whereas, for a specific modulus ratio $\overline{E}_f/\overline{E}_s$, the compressibility increases with enhancement of initial length l_0/H. Finally, as a basis for further investigation and validation of the fungibility of the proposed theoretical framework, we provide and demonstrate the evolution rules regarding compressibility of strain-limiting wrinkled kirigami, i.e., the rules based on peak strain calculation ($\varepsilon_{com-peak}$, see SI Appendix Note 6 and Note 7, for details) and stability analysis ($\varepsilon_{com-stability}$, see SI Appendix Note 7, for details), as evident from Fig. 8c and Fig. E2 (see SI Appendix Note 7, for details). It can be seen from the plots that the larger prestrain can lead to larger compressibility. With increasing of H/h and $\overline{E}_f/\overline{E}_s$, the compressibility via peak strain calculation will increase and decrease, respectively, which can compare favorably with the typical evolutions in Fig. 8a and Fig. 8b. More importantly, for the specific geometric parameters (such as $\varepsilon_p = 0.4$ and $l_0 = 30mm$), the compressibility, in principle, is always equal to $min\{\varepsilon_{com-stability}, \varepsilon_{com-peak}\}$, which the corresponding landscape can be found in Fig. 8c for the yellow space.

4. Conclusions

We have applied closed-form analytical solutions, based on plane-strain composite beam theory, LCCB theory, energy approach, buckling theory regarding finite deformations and geometric nonlinearities, FEM calculations and experiments to demonstrate the effects of different dimensionless parameters on the normalized flexibility, normalized stretchability, and normalized compressibility of strain-limiting wrinkled kirigami materials in a systematic manner. The accuracy of analytical solutions and postbuckling process is validated by combining the FEM and in-situ tension experiments. This study shows that large normalized flexibility and stretchability can be strongly influenced by de-bending effect, de-wrinkle effect and de-prestrain effect, normalized compressibility is attributed to the peak strain, and the compressibility of strain-limiting wrinkled kirigami with geometrically imperfect considerations can be manipulated for a desired response based on stability analysis. The flexibility, stretchability and compressibility, with some rare exceptions, can be enhanced by several orders of magnitude through systematic parameterization investigations. Based on these findings and design strategy associated with highly parallel global buckling and local wrinkling, the broader scope of dimensionless parameters and resultant database can be effective in speed-up of searching the higher flexibility, stretchability and compressibility for stain-limiting wrinkled kirigami materials. The results obtained in this paper develop the design space of existing materials with coexisting high flexibility, stretchability and compressibility, and hold promising potential for practical applications in flexible and stretchable conductors and piezoelectric harvesters.

Declaration of Competing Interest

The authors declare that they have no known competing financial interests or personal relationships that could have appeared to influence the work reported in this paper.

Appendix A. Supplementary data

Supplementary data to this article can be found online at https://doi.org/10.1016/j.ijsolstr.2021.111382.

References

Audoly, B., Boudaoud, A., 2008. Buckling of a stiff film bound to a compliant substrate—Part I. J. Mech. Phys. Solids 56 (7), 2401–2421.

Bai, K., Cheng, X., Xue, Z.G., Song, H.L., Sang, L., Zhang, F., Liu, F., Luo, X., Huang, W., Huang, Y.G., Zhang, Y.H., 2020. Geometrically reconfigurable 3D mesostructures and electromagnetic devices through a rational bottom-up design strategy. Sci. Adv. 6.

Cai, S., Breid, D., Crosby, A.J., Suo, Z., Hutchinson, J.W., 2011. Periodic patterns and energy states of buckled films on compliant substrates. J. Mech. Phys. Solids 59 (5), 1094–1114.

Callens, S.J.P., Zadpoor, A.A., 2018. From flat sheets to curved geometries: origami and kirigami approaches. Mater. Today 21 (3), 241–264.

Cao, Y.-P., Jia, F., Zhao, Y., Feng, X.-Q., Yu, S.-W., 2012. Buckling and post-buckling of a stiff film resting on an elastic graded substrate. Int. J. Solids Struct. 49 (13), 1656–1664.

Carpi, F., Bauer, S., De Rossi, D., 2010. Materials science. Stretching dielectric elastomer performance. Science 330 (6012), 1759–1761.

Chen, X., Hutchinson, J.W., 2004. Herringbone buckling patterns of compressed thin films on compliant substrates. J. Appl. Mech. 71, 597–603.

Chung, H.U., Rwei, A.Y., Hourlier-Fargette, A., Xu, S., Lee, K., Dunne, E.C., Xie, Z., Liu, C., Carlini, A., Kim, D.H., Ryu, D., Kulikova, E., Cao, J., Odland, I.C., Fields, K.B., Hopkins, B., Banks, A., Ogle, C., Grande, D., Park, J.B., Kim, J., Irie, M., Jang, H., Lee, J., Park, Y., Kim, J., Jo, H.H., Hahm, H., Avila, R., Xu, Y., Namkoong, M., Kwak, J.W., Suen, E., Paulus, M.A., Kim, R.J., Parsons, B.V., Human, K.A., Kim, S.S., Patel, M., Reuther, W., Kim, H.S., Lee, S.H., Leedle, J.D., Yun, Y., Rigali, S., Son, T., Jung, I., Arafa, H., Soundararajan, V.R., Ollech, A., Shukla, A., Bradley, A., Schau, M., Rand, C.M., Marsillio, L.E., Harris, Z.L., Huang, Y., Hamvas, A., Paller, A. S., Weese-Mayer, D.E., Lee, J.Y., Rogers, J.A., 2020. Skin-interfaced biosensors for advanced wireless physiological monitoring in neonatal and pediatric intensive-care units. Nat. Med. 26 (3), 418–429.

Efimenko, K., Rackaitis, M., Manias, E., Vaziri, A., Mahadevan, L., Genzer, J., 2005. Nested self-similar wrinkling patterns in skins. Nat. Mater. 4 (4), 293–297.

Fan, Z., Yang, Y., Zhang, F., Xu, Z., Zhao, H., Wang, T., Song, H., Huang, Y., Rogers, J.A., Zhang, Y., 2020. Inverse design strategies for 3D surfaces formed by mechanically guided assembly. Adv. Mater. 32 (14), 1908424. https://doi.org/10.1002/adma.201908424.

Groenewold, J., 2001. Wrinkling of plates coupled with soft elastic media. Phys. A 298 (1-2), 32–45.

Guan, Y.-S., Zhang, Z., Tang, Y., Yin, J., Ren, S., 2018. Kirigami-inspired nanoconfined polymer conducting nanosheets with 2000% stretchability. Adv. Mater. 30 (20), 1706390. https://doi.org/10.1002/adma.201706390.

Harrison, C., Stafford, C.M., Zhang, W., Karim, A., 2004. Sinusoidal phase grating created by a tunably buckled surface. Appl. Phys. Lett. 85 (18), 4016–4018.

Holmes, D.P., 2019. Elasticity and stability of shape-shifting structures. Curr. Opin. Colloid. In. 40, 118–137.

Hou, Y., Zhang, J., Wang, C., Tan, H., Zhang, L., 2021. A spectrum-based inversion method for the evaluation of nanoscale wrinkling amplitude. Phys. E 127, 114512. https://doi.org/10.1016/j.physe.2020.114512.

Huang, R., 2005. Kinetic wrinkling of an elastic film on a viscoelastic substrate. J. Mech. Phys. Solids 53 (1), 63–89.

Huang, R., Im, S.H., 2006. Dynamics of wrinkle growth and coarsening in stressed thin films. Phys. Rev. E 74 (2). https://doi.org/10.1103/PhysRevE.74.026214.

Huang, R., Suo, Z., 2002. Instability of a compressed elastic film on a viscous layer. Int. J. Solids Struct. 39 (7), 1791–1802.

Huang, S.-Q., Li, Q.-Y., Feng, X.-Q., Yu, S.-W., 2006. Pattern instability of a soft elastic thin film under van der Waals forces. Mech. Mater. 38 (1-2), 88–99.

Huang, Z.Y., Hong, W., Suo, Z., 2005. Nonlinear analyses of wrinkles in a film bonded to a compliant substrate. J. Mech. Phys. Solids 53 (9), 2101–2118.

Jang, N.-S., Kim, K.-H., Ha, S.-H., Jung, S.-H., Lee, H.M., Kim, J.-M., 2017. Simple approach to high-performance stretchable heaters based on kirigami patterning of conductive paper for wearable thermotherapy applications. ACS Appl. Mater. Inter. 9 (23), 19612–19621.

Jeong, J.-W., Yeo, W.-H., Akhtar, A., Norton, J.J.S., Kwack, Y.-J., Li, S., Jung, S.-Y., Su, Y., Lee, W., Xia, J., Cheng, H., Huang, Y., Choi, W.-S., Bretl, T., Rogers, J.A., 2013. Materials and optimized designs for human-machine interfaces via epidermal electronics. Adv. Mater. 25 (47), 6839–6846.

Jiang, H., Khang, D.-Y., Song, J., Sun, Y., Huang, Y., Rogers, J.A., 2007. Finite deformation mechanics in buckled thin films on compliant supports. Proc. Natl. Acad. Sci. USA 104 (40), 15607–15612.

Khang, D.-Y., Jiang, H., Huang, Y., Rogers, J.A., 2006. A stretchable form of single-crystal silicon for high-performance electronics on rubber substrates. Science 311 (5758), 208–212.

Kim, D.-H., Ahn, J.-H., Choi, W.M., Kim, H.-S., Kim, T.-H., Song, J., Huang, Y.Y., Liu, Z., Lu, C., Rogers, J.A., 2008a. Stretchable and foldable silicon integrated circuits. Science 320 (5875), 507–511.

Kim, D.-H., Lu, N., Ma, R., Kim, Y.-S., Kim, R.-H., Wang, S., Wu, J., Won, S.M., Tao, H., Islam, A., Yu, K.J., Kim, T.-i., Chowdhury, R., Ying, M., Xu, L., Li, M., Chung, H.-J., Keum, H., McCormick, M., Liu, P., Zhang, Y.-W., Omenetto, F.G., Huang, Y., Coleman, T., Rogers, J.A., 2011. Epidermal electronics. Science 333 (6044), 838–843.

Kim, D.-H., Song, J., Choi, W.M., Kim, H.-S., Kim, R.-H., Liu, Z., Huang, Y.Y., Hwang, K.-C., Zhang, Y.-w., Rogers, J.A., 2008b. Materials and noncoplanar mesh designs for integrated circuits with linear elastic responses to extreme mechanical deformations. Proc. Natl. Acad. Sci. USA 105 (48), 18675–18680.

Ko, H.C., Stoykovich, M.P., Song, J., Malyarchuk, V., Choi, W.M., Yu, C.-J., Geddes III, J. B., Xiao, J., Wang, S., Huang, Y., Rogers, J.A., 2008. A hemispherical electronic eye camera based on compressible silicon optoelectronics. Nature 454 (7205), 748–753.

Li, B., Cao, Y.-P., Feng, X.-Q., Gao, H., 2012. Mechanics of morphological instabilities and surface wrinkling in soft materials: a review. Soft Matter 8 (21), 5728. https://doi.org/10.1039/c2sm00011c.

Liu, Y., Guo, K., Wang, C., Gao, H., 2019. Wrinkling and ratcheting of a thin film on cyclically deforming plastic substrate: mechanical instability of the solid-electrolyte interphase in Li–ion batteries. J. Mech. Phys. Solids 123, 103–118.

Liu, Y., Yan, Z., Lin, Q., Guo, X., Han, M., Nan, K., Hwang, K.C., Huang, Y., Zhang, Y., Rogers, J.A., 2016. Guided formation of 3D helical mesostructures by mechanical buckling: analytical modeling and experimental validation. Adv. Funct. Mater. 26, 2909–2918.

Lu, N., Yang, S., 2015. Mechanics for stretchable sensors. Curr. Opin. Solid. St. M. 19, 149–159.

Ma, R., Wu, C., Wang, Z.L., Tsukruk, V.V., 2018. Pop-up conducting large-area Biographene Kirigami. ACS Nano 12, 9714–9720.

Ma, Y., Feng, X., Rogers, J.A., Huang, Y., Zhang, Y., 2017. Design and application of 'J-shaped' stress-strain behavior in stretchable electronics: a review. Lab Chip 17, 1689–1704.

Ma, Y., Jang, K.I., Wang, L., Jung, H.N., Kwak, J.W., Xue, Y., Chen, H., Yang, Y., Shi, D., Feng, X.P., Rogers, J.A.P., Huang, Y.P., 2016a. Design of strain-limiting substrate materials for stretchable and flexible electronics. Adv. Funct. Mater. 26, 5345–5351.

Ma, Y., Xue, Y., Jang, K.I., Feng, X., Rogers, J.A., Huang, Y., 2016b. Wrinkling of a stiff thin film bonded to a pre-strained, compliant substrate with finite thickness. Proc. Math. Phys. Eng. Sci. 472, 20160339.

Mannsfeld, S.C., Tee, B.C., Stoltenberg, R.M., Chen, C.V., Barman, S., Muir, B.V., Sokolov, A.N., Reese, C., Bao, Z., 2010. Highly sensitive flexible pressure sensors with microstructured rubber dielectric layers. Nat. Mater. 9, 859–864.

Mei, H., Landis, C.M., Huang, R., 2011. Concomitant wrinkling and buckle-delamination of elastic thin films on compliant substrates. Mech. Mater. 43, 627–642.

Rogers, J.A., Someya, T., Huang, Y., 2010. Materials and mechanics for stretchable electronics. Science 327, 1603–1607.

Shyu, T.C., Damasceno, P.F., Dodd, P.M., Lamoureux, A., Xu, L., Shlian, M., Shtein, M., Glotzer, S.C., Kotov, N.A., 2015. A kirigami approach to engineering elasticity in nanocomposites through patterned defects. Nat. Mater. 14, 785–789.

Someya, T., Sekitani, T., Iba, S., Kato, Y., Kawaguchi, H., Sakurai, T., 2004. A large-area, flexible pressure sensor matrix with organic field-effect transistors for artificial skin applications. Proc. Natl. Acad. Sci. USA 101, 9966–9970.

Song, J., 2015. Mechanics of stretchable electronics. Curr. Opin. Solid St. M. 19, 160–170.

Song, J., Feng, X., Huang, Y., 2016. Mechanics and thermal management of stretchable inorganic electronics. Natl. Sci. Rev. 3, 128–143.

Stafford, C.M., Harrison, C., Beers, K.L., Karim, A., Amis, E.J., VanLandingham, M.R., Kim, H.C., Volksen, W., Miller, R.D., Simonyi, E.E., 2004. A buckling-based metrology for measuring the elastic moduli of polymeric thin films. Nat. Mater. 3, 545–550.

Sun, J.Y., Xia, S., Moon, M.W., Oh, K.H., Kim, K.S., 2011. Folding wrinkles of a thin stiff layer on a soft substrate. Proc. Roy. Soc. A 468, 932–953.

Sun, Y., Choi, W.M., Jiang, H., Huang, Y.Y., Rogers, J.A., 2006. Controlled buckling of semiconductor nanoribbons for stretchable electronics. Nat. Nanotechnol. 1, 201–207.

Timoshenko, S.P., Goodier, J.N.J.J.o.A.M., 1970. Theory of Elasticity (3rd ed.). 37, 888.

Wagner, S., Lacour, S.P., Jones, J., Hsu, P.-h.I., Sturm, J.C., Li, T., Suo, Z., 2004. Electronic skin: architecture and components. Phys. E 25, 326–334.

Wang, C.G., Liu, Y.P., Tan, H.F., 2016. Global and local interactive buckling behavior of a stiff film/compliant substrate system. Int. J. Solids Struct. 102–103, 176–185.

Wang, S., Li, M., Wu, J., Kim, D.H., Lu, N., Su, Y., Kang, Z., Huang, Y., Rogers, J.A., 2012. Mechanics of Epidermal Electronics. J. Appl. Mech. 79.

Wang, S., Song, J., Kim, D.H., Huang, Y., Rogers, J.A., 2008. Local versus global buckling of thin films on elastomeric substrates. Appl. Phys. Lett. 93.

Wang, Y., Wang, C., 2020. Buckling of ultrastretchable kirigami metastructures for mechanical programmability and energy harvesting. Int. J. Solids Struct. 213, 93–102.

Wang, Y., Wang, C., Tan, H., 2020. Geometry-dependent stretchability and stiffness of ribbon kirigami based on large curvature curved beam model. Int. J. Solids Struct. 182–183, 236–253.

Wu, Z., Bouklas, N., Liu, Y., Huang, R., 2017. Onset of swell-induced surface instability of hydrogel layers with depth-wise graded material properties. Mech. Mater. 105, 138–147.

Xu, F., Koutsawa, Y., Potier-Ferry, M., Belouettar, S., 2015a. Instabilities in thin films on hyperelastic substrates by 3D finite elements. Int. J. Solids Struct. 69–70, 71–85.

Xu, F., Potier-Ferry, M., Belouettar, S., Cong, Y., 2014. 3D finite element modeling for instabilities in thin films on soft substrates. Int. J. Solids Struct. 51, 3619–3632.

Xu, S., Yan, Z., Jang, K.I., Huang, W., Fu, H.R., Kim, J., Wei, Z., Flavin, M., McCracken, J., Wang, R., Badea, A., Liu, Y., Xiao, D.Q., Zhou, G.Y., Lee, J., Chung, H. U., Cheng, H.Y., Ren, W., Banks, A., Li, X.L., Paik, U., Nuzzo, R.G., Huang, Y.G., Zhang, Y.H., Rogers, J.A., 2015b. Assembly of micro/nanomaterials into complex, three-dimensional architectures by compressive buckling. Science 347, 154–159.

Yan, Z.G., Wang, B.L., Wang, K.F., 2019. Stretchability and compressibility of a novel layout design for flexible electronics based on bended wrinkle geometries. Compos. Part B 166, 65–73.

Yang, C., Suo, Z., 2018. Hydrogel ionotronics. Nat. Rev. Mater. 3, 125–142.

Yeo, W.H., Kim, Y.S., Lee, J., Ameen, A., Shi, L., Li, M., Wang, S., Ma, R., Jin, S.H., Kang, Z., Huang, Y., Rogers, J.A., 2013. Multifunctional epidermal electronics printed directly onto the skin. Adv. Mater. 25, 2773–2778.

Zhang, Y., Fu, H., Su, Y., Xu, S., Cheng, H., Fan, J.A., Hwang, K.-C., Rogers, J.A., Huang, Y., 2013. Mechanics of ultra-stretchable self-similar serpentine interconnects. Acta Mater. 61, 7816–7827.

Zhang, Y., Huang, H., Rogers, J.A., 2015a. Mechanics of stretchable batteries and supercapacitors. Curr. Opin. Solid. St. M. 19, 190–199.

Zhang, Y., Yan, Z., Nan, K., Xiao, D., Liu, Y., Luan, H., Fu, H., Wang, X., Yang, Q., Wang, J., Ren, W., Si, H., Liu, F., Yang, L., Li, H., Wang, J., Guo, X., Luo, H., Wang, L., Huang, Y., Rogers, J.A., 2015b. A mechanically driven form of Kirigami as a route to 3D mesostructures in micro/nanomembranes. Proc. Natl. Acad. Sci. USA 112, 11757–11764.